Vertical cloud structures of the boreal summer intraseasonal variability based on CloudSat observations and ERA-interim reanalysis

Xianan Jiang · Duane E. Waliser · Jui-Lin Li · Christopher Woods

Abstract The boreal summer intraseasonal variability (BSISV), which is characterized by pronounced meridional propagation from the equatorial zone to the Indian Continent, exerts significant modulation of the active/break phases of the south Asian monsoon. This form of variability provides a primary source of subseasonal predictive skill of the Asian summer monsoon. Unfortunately, current general circulation models display large deficiencies in representing this variability. The new cloud observations made available by the CloudSat mission provide an unprecedented opportunity to advance our characterization of the BSISV. In this study, the vertical structures of cloud water content and cloud types associated with the BSISV over the Indian Ocean and subcontinent are analyzed based on CloudSat observations from 2006 to 2008. These cloud structures are also compared to their counterparts as derived from ERA-interim reanalysis. A marked vertical tilting structure in cloud water is illustrated during the northward propagation of the BSISV based on both datasets. Increased cloud liquid water content (LWC) tends to appear to the north of the rainfall maximum, while ice water content (IWC) in the upper troposphere slightly lags the convection. This northward shift of increased LWC, which is in accord with local enhanced moisture as previously documented, may play an important role in the northward propagation of the BSISV. The transition in cloud structures associated with BSISV convection is further demonstrated based on CloudSat, with shallow cumuli at the leading edge, followed by the deep convective clouds, and then upper anvil clouds. Some differences in cloud water structures between CloudSat and ERA-interim are also noted, particularly in the amplitudes of IWC and LWC fields.

Keywords Intraseasonal variability · Cloud water · Northward propagation · CloudSat

1 Introduction

It has been widely acknowledged that the intraseasonal variability (ISV) plays a significant role for tropical climate (see recent reviews by Lau and Waliser 2005; Zhang 2005; Wang 2006). While the eastward propagating Madden–Julian Oscillation (MJO; Madden and Julian 1971, 1994) is found to be a dominant ISV form in boreal winter, the boreal summer ISV (BSISV), with a period of 30–50 days, is characterized by a pronounced northward propagation over the Asian monsoon region (e.g., Yasunari 1979; Hsu and Weng 2001; Lawrence and Webster 2002; Hsu et al. 2004; Jiang et al. 2004; Jiang and Li 2005; Goswami 2005; Wang et al. 2005; Waliser 2006; and many others). The meridional propagation of the BSISV is found to be intimately associated with active and break phases of the Asian summer monsoon (e.g., Sikka and Gadgil 1980; Cadet 1986; Lawrence and Webster 2002). Due to its quasi-periodic occurrence, the BSISV provides a primary source for the predictability of the Asian monsoon on

X. Jiang · D. E. Waliser
Joint Institute for Regional Earth System Science and
Engineering, University of California, Los Angeles, California

X. Jiang (✉) · D. E. Waliser · J.-L. Li · C. Woods
Jet Propulsion Laboratory, California Institute of Technology,
MS 183-501, 4800 Oak Grove Drive, Pasadena, CA 91109, USA
e-mail: xianan@jifresse.ucla.edu

Present Address:
C. Woods
The Aerospace Corporation, El Segundo, CA, USA

 Springer

subseasonal time scales, and thus has received significant attention in the climate research community.

A number of theories have been advanced in interpreting this northward propagating BSISV, including the land–atmosphere interaction (Webster 1983), Rossby wave emanation from the eastward propagating equatorial Kelvin–Rossby wave packet (Wang and Xie 1997; Lawrence and Webster 2002), and air–sea interactions (Kemball-Cook and Wang 2001; Fu et al. 2003). Based on analyses of both an atmospheric general circulation model (GCM) simulation and reanalysis dataset, Jiang et al. (2004) identified prominent meridional asymmetric structures associated with the northward propagating BSISV. A positive equivalent barotropic vorticity perturbation and enhanced specific humidity in the lower troposphere are found to lead the convection center by a few degrees. The northward shift of low-level moisture perturbation relative to the BSISV convection, which may suggest a pre-conditioning process for its northward propagation, has also been illustrated by other observational studies (e.g., Hsu et al. 2004; Fu et al. 2006). Jiang et al. (2004) further proposed an "*easterly vertical wind shear*" mechanism to explain the northward propagation of the BSISV, in which the easterly vertical shear of the zonal mean flow over the Asian monsoon region could play a fundamental role. This mechanism was confirmed by a numerical study based on an idealized model (Drbohlav and Wang 2005). Most recently, this "*easterly vertical wind shear*" mechanism was further verified by inspecting the meridional propagation of the ISV over the eastern Pacific warm pool region (Jiang and Waliser 2008, 2009).

While great progress has been made to gain a better understanding of the BSISV during the past decades, complete interpretation of the BSISV phenomena remains elusive, including the mechanisms for its initiation and temporal/spatial-scale selection, as well as detailed evolution patterns. Moreover, the ability to properly represent this form of variability remains a great challenge to current weather/climate models (e.g., Waliser et al. 2003; Wang 2008; Kim et al. 2008). It is generally agreed that the poor representation of this variability in current models could be largely ascribed to the lack of the interaction between the large-scale circulation and small-scale convective processes, the latter of which are not explicitly resolved in current conventional GCMs, and can only be realized via so-called "parameterization" approaches.

In recent years, the cloud structure information made available based on remote-sensing techniques provides great insights into convective processes coupled with the large-scale circulation. For example, distinct cloud regimes associated with "weather states" were investigated based on International Satellite Cloud Climatology Project (ISCCP) D1 data (e.g., Jakob and Tselioudis 2003; Rossow et al. 2005;

Chen and Del Genio 2009; Tromeur and Rossow 2010). In particular, Chen and Del Genio (2009) and Tromeur and Rossow (2010) analyzed the frequency of occurrence of each cloud regime during the evolution of the MJO. Their results confirm the important role of cumulus congestus clouds for the pre-conditioning of MJO deep convection as previously proposed (e.g., Johnson et al. 1999; Kikuchi and Takayabu 2004). While the ISCCP D1 data provide valuable information regarding the coupling between convection and dynamics, the major limitation is the lack of detailed information on cloud vertical structures, which is a common shortcoming of passive sensor measurements.

The recent CloudSat satellite radar mission provides an unprecedented opportunity to explore the three-dimensional cloud structures associated with the large-scale circulation, including that associated with the ISV. In the present study, vertical cloud water structures associated with the northward propagation of the BSISV are examined by utilizing cloud liquid and ice water content fields based on CloudSat estimates. These features are also compared to their counterparts from the European Centre for Medium-Range Weather Forecast (ECMWF) ERA-interim reanalysis. The cloud classification information provided by CloudSat will also be analyzed to understand the cloud water structures. Due to the limited period of CloudSat observations available at the time of this study, we will mainly focus on the analyses for three summer seasons from 2006 to 2008. The organization of this paper is as follows. The datasets employed in this study are described in Sect. 2. In Sect. 3, an objective approach to identify strong northward propagating BSISV events is introduced. In Sect. 4, vertical cloud structures associated with the BSISV are analyzed based on a composite analysis by using both CloudSat observations and ERA-interim reanalysis. Finally, a summary and a discussion are given in Sect. 5.

2 Datasets

The primary dataset used for this study is the cloud liquid and ice water contents based on CloudSat estimates since its launch in 2006 as part of the NASA A-Train constellation of satellites (Stephens et al. 2002). The Cloud Profiling Radar (CPR) on the CloudSat satellite is a 94 GHz, nadir-viewing radar measuring backscattered power from clouds and precipitation particles in the atmospheric column within a 1.4 km across-track by 2.5 km along-track radar footprint. Measurements of radar backscatter are converted to a calibrated radar reflectivity factor, which is then used in estimates of cloud and precipitation properties, such as profiles of liquid water content (LWC) and ice water content (IWC). The minimum detectable reflectivity is approximately -30 dBZ.

The cloud LWC and IWC employed in this study are generated by the latest CloudSat retrieval algorithm (version 5.1, contained in release 4 of the CloudSat 2B-CWC-RO data product), which uses an optimal estimation approach to retrieve parameters of the cloud particle size distribution based on measurements of radar reflectivity (Austin et al. 2009). The cloud water estimates are obtained by constraining LWC values only in regions warmer than 0 °C, the IWC in regions colder than −20 °C, and a linear combination of the two in the intermediate temperature range. The LWC and IWC provided by the CloudSat dataset are interpolated onto grids with $1 \times 1°$ horizontal resolution and 40 vertical levels between 1,025 and 50 hPa.

We also utilize CloudSat determinations of cloud types, including stratus (St), stratocumulus (Sc), cumulus (Cu), nimbostratus (Ns), altocumulus (Ac), altostratus (As), deep convective clouds (Dc), and high cirrus/cirrostratus clouds (Ci). These determinations are based on different rules for hydrometeor vertical and horizontal scales, the maximum effective radar reflectivity factor measured by the CloudSat CPR, and ancillary data including predicted ECMWF temperature profiles (Wang and Sassen 2007; Sassen and Wang 2008).

ERA-interim reanalysis LWC and IWC are also examined to facilitate comparison to those from the CloudSat observations. The ERA-interim, which is the latest ECMWF reanalysis (Simmons et al. 2006), benefits from several developments of the ECMWF integrated forecasting system, including improved model physics, a new humidity analysis, the use of a 4D-VAR assimilation scheme, a variational bias correction technique, and direct assimilation of early satellite radiance data. The LWC and IWC fields based on ERA-interim reanalysis extend from 1989 to present with 1.5° horizontal resolution and 37 vertical pressure levels. Since CloudSat observations are only available since 2006, we will focus our analysis on the period of 2006–2008 based on both the CloudSat dataset and ERA-interim. Note that CloudSat was not used in the assimilation for the ERA-interim reanalysis.

Rainfall observations based on Tropical Rainfall Measuring Mission (TRMM, version 3B42; Huffman et al. 2007) are employed to identify the BSISV events. TRMM 3B42 is a global precipitation product based on multi-satellite and rain gauge analyses. It provides precipitation estimates gridded on a 3-hourly temporal resolution and a 0.25° spatial resolution in a global belt extending from 50°S to 50°N.

3 An index for the boreal summer intraseasonal variability

Daily mean rainfall from 1998 to 2008 with a horizontal resolution of $1 \times 1°$ is first calculated based on the raw TRMM 3B42 dataset, and is subject to Lanczos band-pass filtering to retain the ISV period of 20–70 days (Duchon 1979). The Hovmöller diagram of the ISV rainfall anomalies over the Indian Ocean (IO) Bay of Bengal (BoB) longitudes (80°–95°E) during the summers from 2006 to 2008 are displayed in Fig. 1a–c. Frequent occurrence of the northward propagation of the BSISV over this region is clearly evident. Next, to objectively select strong BSISV events and determine their phases, an extended empirical orthogonal function (EEOF) analysis (Weare and Nasstrom 1982) is conducted based on daily band-pass filtered one-dimensional rainfall data over the BoB sector from June 1 to September 30 of 1998–2008, where the daily rainfall data is derived by averaging over 80°–95°E, with 22 spatial points between 0.5°N and 21.5°N at 1° resolution. The EEOF analysis is performed with 21 temporal lags. Results indicate that the first two leading EEOF modes are in quadrature with each other; both of them represent the same northward propagating BSISV mode. These two leading EEOFs explain 62% of total variance of anomalous rainfall and are well separated from higher order modes based on North et al.'s (1982) criterion (figure not shown).

Time series of $EEOF_1$ during June–September from 2006 to 2008 are displayed in Fig. 1d–f. The northward propagation BSISV events as illustrated by the Hovmöller diagrams in Fig. 1a–c correspond well to positive peaks in $EEOF_1$, with the timing of each peak in $EEOF_1$ representing enhanced BSISV convective conditions near the equator. We then define strong northward propagating BSISV events by selecting maximum peaks in $EEOF_1$ time series exceeding 0.8. By doing so, 10 relatively strong northward propagation events are identified during the three summers as denoted by dark dots in Fig. 1d–f. The time corresponding to each of these selected peaks is taken as reference "day 0" of each event for the following composite analysis.

Figure 2 shows the Hovmöller diagram of composite rainfall anomalies over the BoB sector based on the 10 selected BSISV events. Days with negative/positive numbers in the abscissa represent the number of days leading/lagging the reference day 0. Clearly evident in this composite Hovmöller diagram is the pronounced northward propagation of rainfall from the equatorial region to the Indian continent with a phase speed of about 1 deg day^{-1}. A weak and short-lived southward propagation signal to the south of the equator is also discernible. The evolution patterns of 2D ISV rainfall anomalies based on the composite are further displayed in Fig. 3, where the rainfall pattern at day −10 represents 5-day averaged values between day −12 and day −8, and day −5 for average between day −7 and day −3, and so on. Between day −10 and day −5, the BSISV signal first appears over the western equatorial IO. It then propagates eastward along the
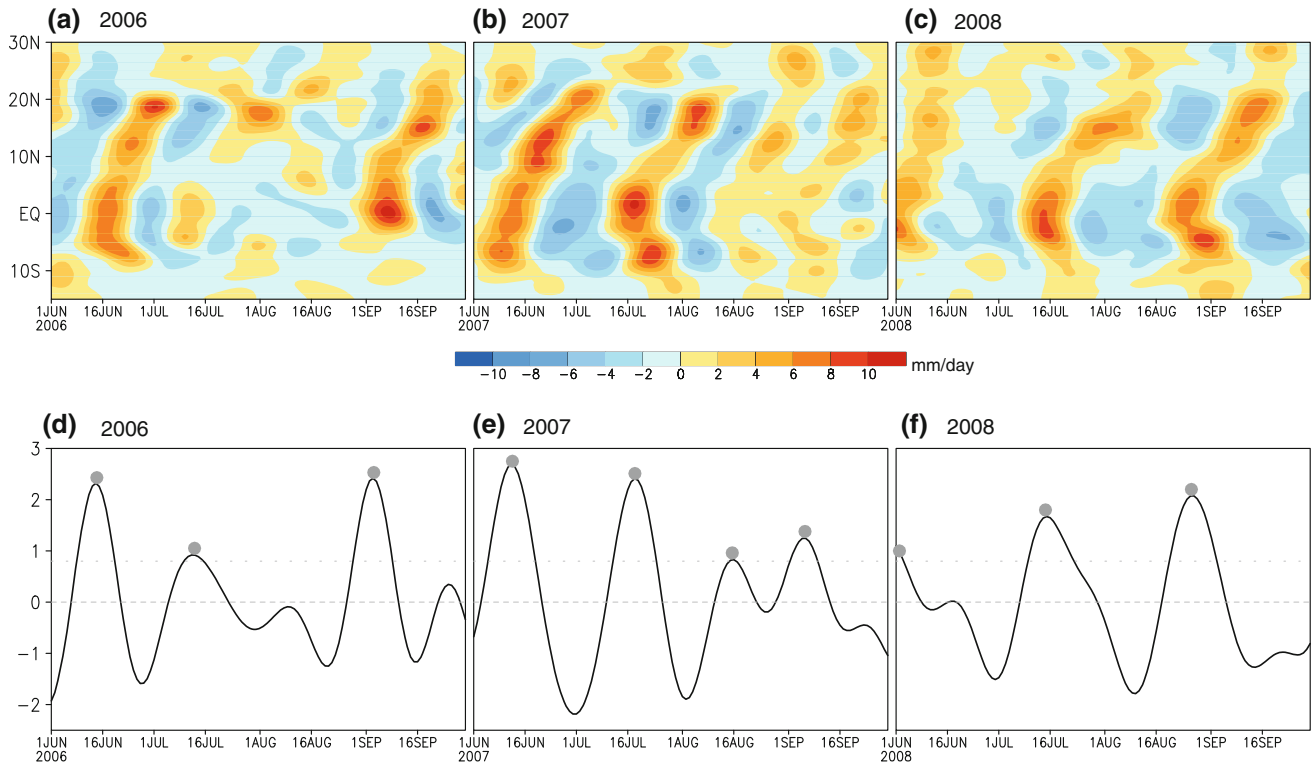
Fig. 1 *Upper panels* Time-latitude diagram of anomalous rainfall over the Indian Ocean Bay of Bengal sector (80°–95°E) during summertime of **a** 2006, **b** 2007, and **c** 2008. See the color bar below with units of mm day^{-1}. *Lower panels* Time series of temporal coefficients for EEOF$_1$ of 2D rainfall over the Indian Ocean during **d** 2006, **e** 2007, and **f** 2008 summers. The *gray dots* denote relatively strong northward propagating BSISV events with coefficients surpassing 0.8 of their standard deviations
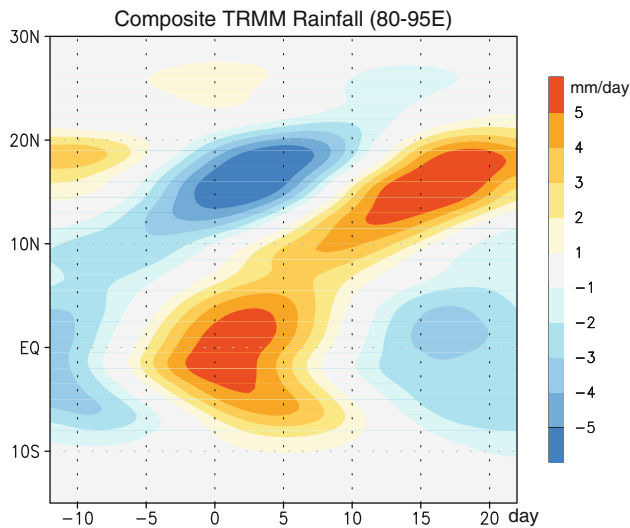
Fig. 2 Time-latitude distribution of composite anomalous rainfall over the BoB sector (80°–95°E) based on 10 strong BSISV events during 2006–2008 (units: mm day^{-1})

equator while intensifying. At day 0, the enhanced BSISV convection is present over the eastern equatorial IO. Subsequently, it bifurcates in the meridional direction with the northern branch of convection migrating toward the Indian Continent, while the southern branch is quickly damped. In conjunction with this meridional movement, eastward propagation of the convection signal along the equator is also evident after day 0, which leads to a southeast-northwestward tilting structure in rainfall anomalies. All these above features of the BSISV greatly resemble those delineated in previous studies (e.g., Lawrence and Webster 2002; Jiang et al. 2004; Jiang and Li 2005; Goswami 2005; Wang et al. 2005; Waliser 2006). Therefore, although the period of datasets employed in this study is limited due to the availability of the CloudSat observations, the results based on the ten strong BSISV events during three recent summers still represent typical characteristics of the BSISV.

4 Vertical cloud structures of the northward propagating BSISV

In this section, we will characterize the cloud structures associated with the BSISV. In particular, we will examine meridional asymmetries in the clouds relative to the BSISV convection center during its northward propagation. Such information would provide insight into the physics responsible for the northward propagation of the BSISV.
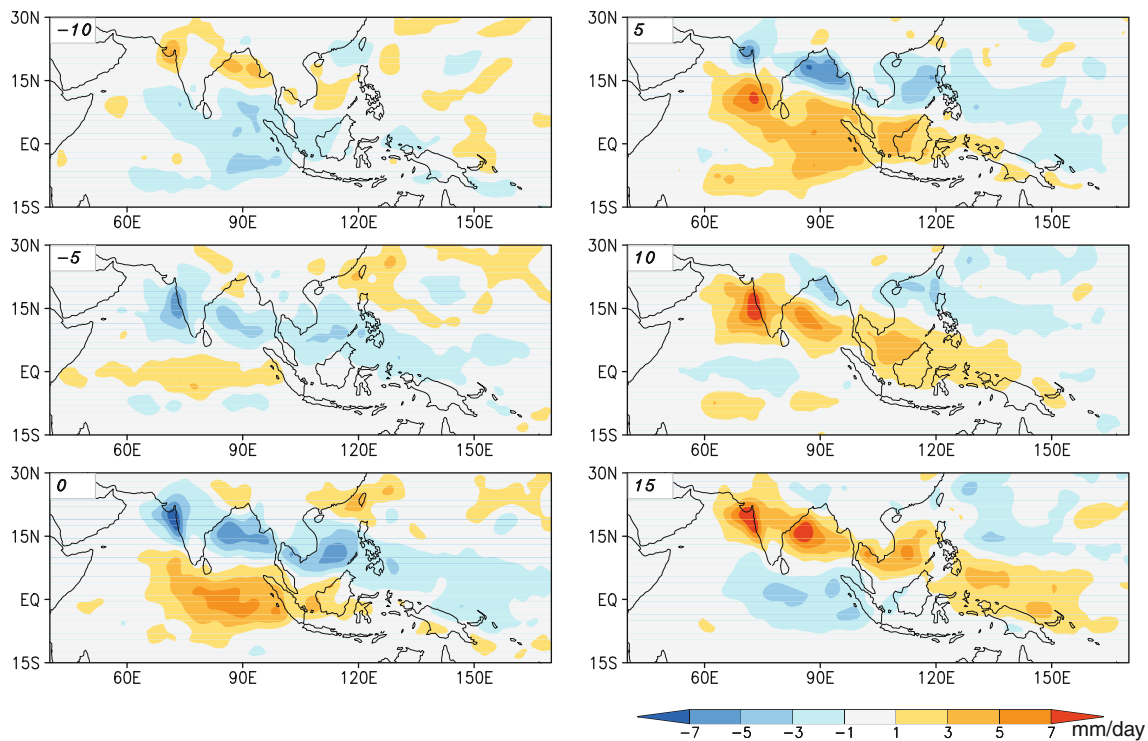
Fig. 3 Evolution of 2D composite anomalous rainfall patterns based on 10 BSISV events during 2006–2008 (units: mm day^{-1})

4.1 Cloud water

Figure 4 shows the time evolution of composite latitude-pressure profiles of CloudSat LWC anomalies over the BoB longitudes (shaded in the upper portion of each panel) at time lags ranging from day −5 to day 20. Note that band-pass filtering has not been applied for daily CloudSat cloud water fields due to quite a number of missing data present on the 1 × 1° grids because of the single sub-orbital footprint of the CloudSat CPR. Instead, only corresponding summer (JJAS) mean values from 2006 to 2008 are removed from total composite fields to highlight ISV perturbations. To clearly present LWC structures relative to the convection center, composite rainfall anomalies over the same BoB sector at each time lag are also displayed in the lower part of each panel in Fig. 4, where green (blue) shading denotes enhanced (suppressed) BSISV convection phases. Consistent with Figs. 2 and 3, a positive rainfall anomaly is located near the equator at day −5. Thereafter, this equatorial positive rainfall anomaly begins to expand meridionally and undergoes northward movement toward the Tibetan Plateau after day 5. In concert with the evolution of the convection, apparent is the northward propagation of positive LWC anomalies in the lower troposphere. The most noteworthy feature in Fig. 4 is the vertical tilting structure of positive LWC anomalies relative to the convection center during the northward movement of the BSISV. Enhanced LWC perturbations are

found to the north of the convection center in the lower troposphere, whereas they are roughly in phase with maximum rainfall anomalies in mid-troposphere. A very similar feature in the anomalous moisture fields associated with the northward propagating BSISV has also been reported in previous studies (e.g., Jiang et al. 2004; Fu et al. 2006), which could be indicative of a pre-conditioning process for the northward propagation of BSISV convection.

Analogous evolution maps of composite CloudSat IWC profiles during the BSISV evolution are presented in Fig. 5. The northward movement of IWC anomalies in the mid- and upper troposphere coupled with the convection is also evident. In spite of some noisy higher-order embedded signals, the IWC anomalies are largely in agreement with surface rainfall anomalies, with enhanced (suppressed) convection generally corresponding to positive (negative) IWC anomalies in the mid- and upper troposphere.

To further substantiate these above cloud water features associated with the northward propagating BSISV based on CloudSat, we further analyze cloud water fields generated by ERA-interim reanalysis. Similar to CloudSat, summer mean cloud water fields from 2006 to 2008 have been removed for ERA-interim to obtain anomalous patterns associated with the BSISV. Profiles of LWC and IWC temporal evolution are shown in Figs. 6 and 7, as in Figs. 4 and 5, but based on the reanalysis. It is particularly intriguing that the vertical tilting structure of LWC during
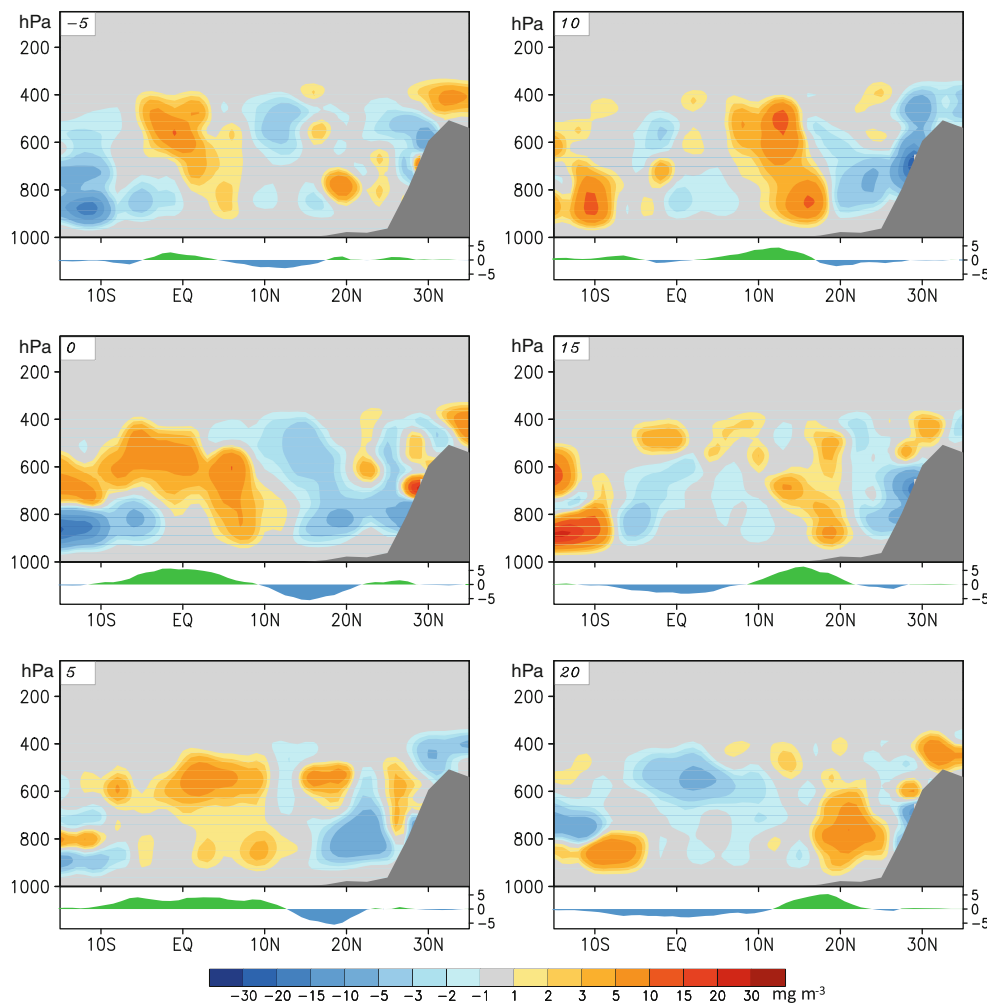
Fig. 4 *Upper part in each panel* Time evolution of pressure-latitude profiles of 5-day mean anomalous CloudSat LWC over the BoB from day −5 to day 20 based on composite analysis over the ten strong BSISV events during 2006–2008 summers (*shaded*; see color scale in the bottom with units of mg m⁻³). *Lower part in each panel* Latitudinal profiles of rainfall at the BoB (see the right coordinate with units of mm day⁻¹). Both LWC and rainfall fields are averaged over 80°–95°E. *Dark shading* in each panel donates the topography of Tibetan Plateau

the northward propagation of the BSISV is also evident in Fig. 6 by the ERA-interim. The northward shift of enhanced LWC anomalies relative to the convection center in the lower troposphere can be clearly seen, particularly during a strong northward propagation period after day 5 (see Fig. 2).

Composite IWC profiles based on the ERA-interim in Fig. 7 also exhibit systematic northward propagation along with the convection. While the upper-level positive (negative) IWC anomalies are largely consistent with enhanced (suppressed) convection as previously discussed in Fig. 5 by CloudSat, a southward shift of the IWC maxima relative to the convection center is also noticeable in Fig. 7, e.g., at days 10 and 15. The ERA-interim composite results exhibit much smoother patterns and more coherent northward propagation than those based on CloudSat, which could be partially due to a greater sample size of ERA-interim.

It is worth mentioning that these aforementioned cloud water features associated with the BSISV based on both CloudSat and ERA-interim datasets are mainly discussed in terms of the enhanced BSISV convection phase (e.g., after day 5 in Figs. 4, 5, 6, 7). Very similar features, including the prominent vertical tilting structure in the LWC relative to the convection center, are also perceptible during the suppressed BSISV period (e.g., between day −5 and 5 in Figs. 4, 5, 6, 7), except with an opposite sign. This further lends confidence to the robustness of these above-mentioned features in cloud water fields associated with the BSISV.

Next, in order to further summarize the meridional IWC and LWC structures associated with the BSISV, daily pressure-latitude profiles of LWC and IWC based on both CloudSat and ERA-interim during the strong northward propagation period of the BSISV (e.g., from day 5 to day 22
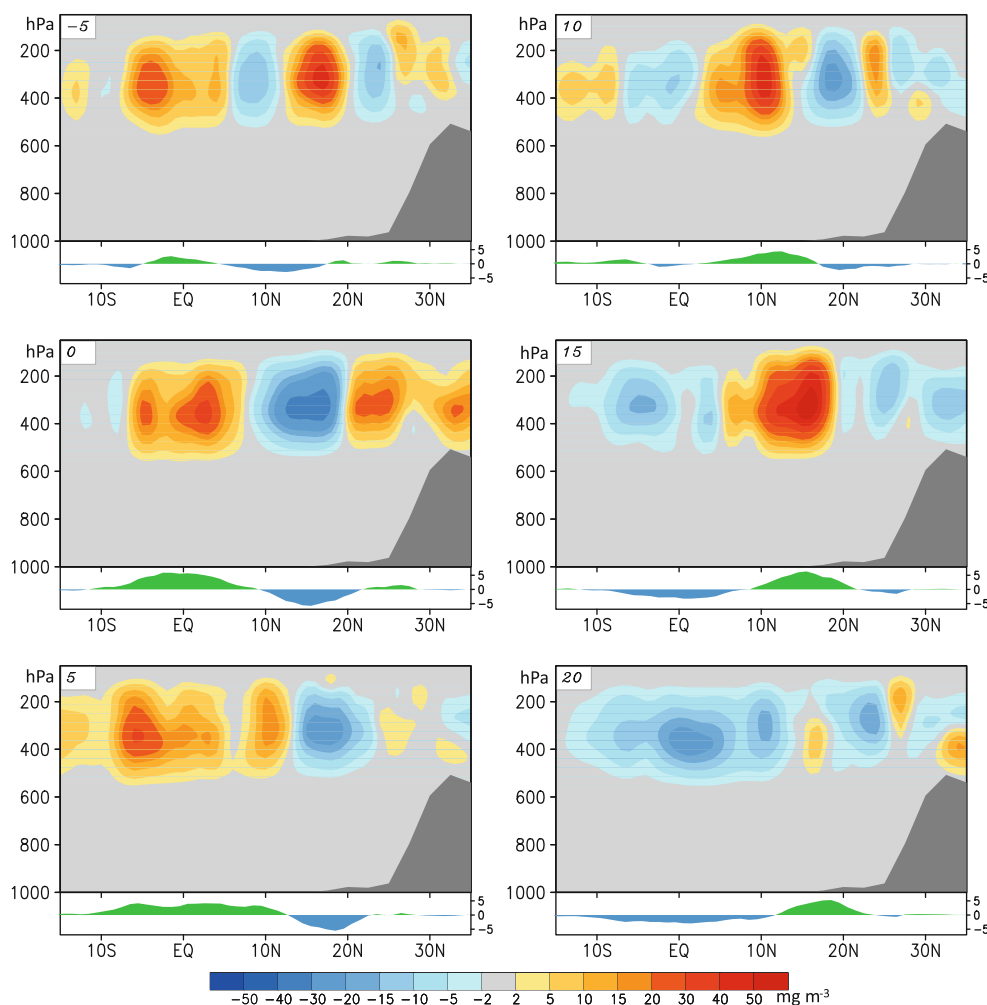
Fig. 5 Same as in Fig. 4, except that the shading in upper portion of each panel represents CloudSat IWC anomalies

as suggested by Fig. 2) are further composited with respect to the reference latitude with maximum rainfall anomalies at each day, and the results are displayed in Fig. 8. A similar composite analysis for the meridional profiles of TRMM rainfall is also conducted and shown in the two lower panels. The x-axis in each panel of Fig. 8 is the relative distance from the convection center (denoted by "0") in degrees of latitude, with positive (negative) values representing north (south) of the center. The pronounced northward shift of the enhanced LWC in the lower troposphere relative to the convection center by about 3°–4° is again clearly evident in both CloudSat (Fig. 8a) and reanalysis (Fig. 8c). Nevertheless, notable differences in the LWC structures are discernible between these two datasets. The maximum LWC anomalies by CloudSat are found to the north of the convection center in the low levels (Fig. 8a); in contrast, ERA-interim maximum LWC anomalies are located in the mid-troposphere (Fig. 8c). Greater

amplitudes of LWC anomalies are also noticeable in the ERA-interim (note the different color scales in Fig. 8a, c).

Meanwhile, maximum IWC anomalies are found aloft near 400 hPa, and are largely coincident with the convection center for CloudSat (Fig. 8b) with only a slight southward shift, but situated about 2° south of the convection center for ERA-interim (Fig. 8d). CloudSat IWC amplitudes are also much larger than those of ERA-interim. Maximum CloudSat IWC anomalies are 30 mg m^{-3} (Fig. 8b), while those based on the reanalysis are only about 12 mg m^{-3}, a factor of two to three times smaller. Other studies have also reported much larger mean IWC magnitudes from CloudSat IWC compared to GCMs (e.g., Li et al. 2007; Waliser et al. 2009; Wu et al. 2009). This could be largely due to the greater CloudSat sensitivity to larger precipitation particles, including snow and graupel, as well as suspended cloud ice. Precipitation particles are not necessarily represented in GCM IWC fields.
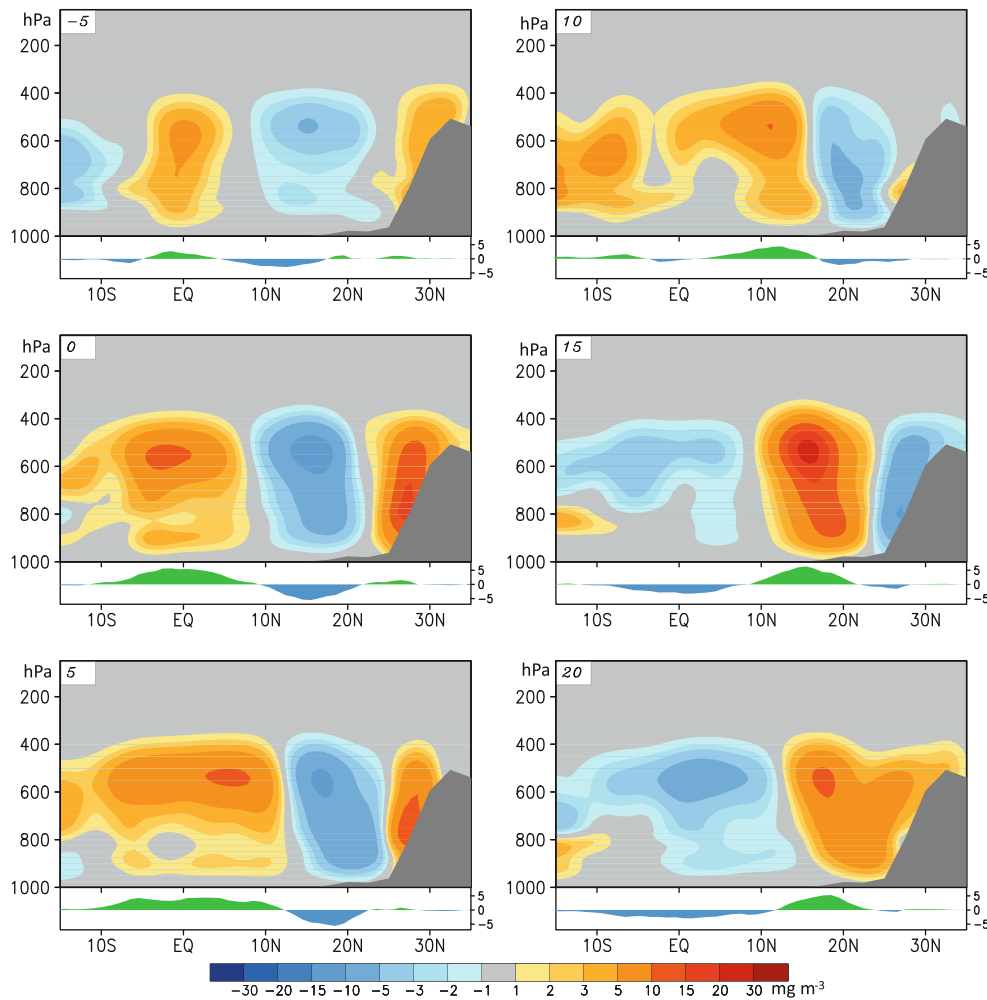
Fig. 6 Same as in Fig. 4, except for LWC based on ERA-interim

4.2 Cloud fractional coverage and cloud classifications

In order to better understand the above cloud water structures of the BSISV, we further examine vertical profiles of cloud fractional coverage from both CloudSat and ERA-interim. Moreover, the contribution from each cloud type to the total anomalous cloud fraction pattern associated with the BSISV is examined with CloudSat cloud classifications.

Similar to Fig. 8a–d, Fig. 9a depicts composite meridional–vertical cloud fraction perturbations relative to the BSISV convection center based on CloudSat (shaded). Increased cloud fractional coverage is consistent with the active convection condition of the BSISV (cf. Fig. 8). Meanwhile, regions with reduced cloud coverage are found on both sides of the active convection. Additionally, the anomalous cloud fraction tilts southward with height. In contrast to a slight southward displacement relative to the convection center of the CloudSat IWC anomalies (Fig. 8b), the cloud fraction anomalies exhibit a significant

southward displacement in the upper troposphere. The southward tilt in the maximum cloud fractional coverage with increasing height is also consistent with the ERA-interim in Fig. 9b, which depicts the meridional profiles of anomalous fractional coverage for low, middle, and high clouds. The maximum cloud cover anomalies of low clouds appear to the north of the convection center, such that shallow clouds lead the convection; middle clouds are more or less in phase, and high clouds lag the convection center.

To shed light on coupling between clouds and the large-scale circulation, the associated vertical-meridional circulation based on ERA-interim is also illustrated by vectors in Fig. 9a. Strong upward motion is intimately associated with enhanced convection and clouds, while regions with reduced cloud coverage are characterized by weak downward motion due to the convective overturning flow. Note that the vertical axis of maximum upward motion also displays a southward tilt with height relative to the convection center. The strongest upward vertical velocity is
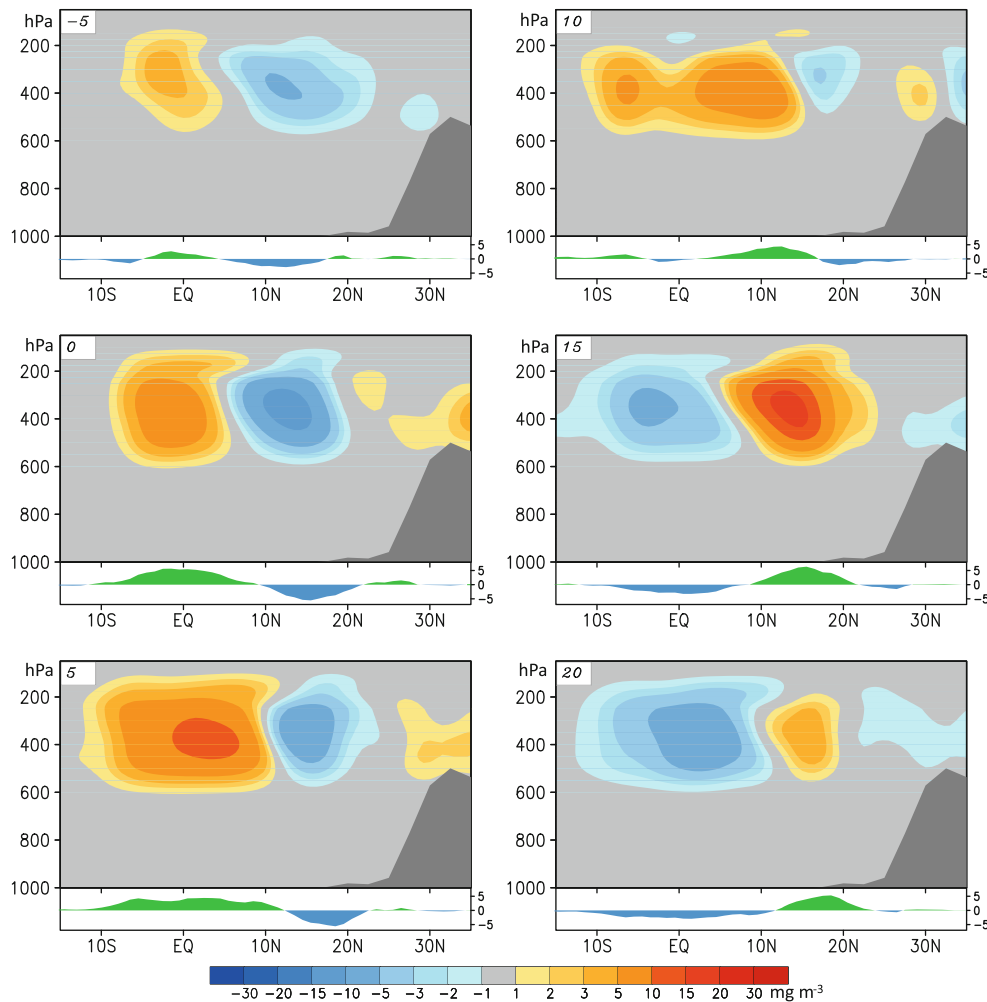
Fig. 7 Same as in Fig. 5, except for IWC based on ERA-interim

largely collocated with the convection center at lower and mid-levels, while it shifts to the south in the upper troposphere. This vertical configuration in cloud and circulation greatly mirrors the typical evolution of individual mesoscale convective systems (MCSs; Houze 2004). The upper-level clouds to the south of the convection center, which are coupled with the divergent outflow, resemble the anvil clouds spreading outward from deep convection.

Figure 10 shows the total anomalous cloud fractional coverage associated with the BSISV (shading in Fig. 9a, and duplicated in Fig. 10a with a modified color scale) decomposed into each cloud type based on CloudSat estimates (Fig. 10b–f). The results suggest that deep convective clouds, which are collocated with the convection center, play a dominant role for the total cloud fraction perturbation (Fig. 10b). The vertical tilting structure in the total anomalous cloud fraction as previously discussed is mainly due to phase shifting relative to the convection center of the mid-to-upper level altostratus (Fig. 10d), mid-level altocumulus (Fig. 10e), and low-level cumulus/

stratocumulus (Fig. 10d) clouds. The Cu/Sc clouds appear ahead of the deep convection, and Ac clouds are roughly in the phase or slightly lag, whereas As clouds significantly lag the convection. The high cirrus/cirrostratus clouds, however, display relatively less well-organized structures (Fig. 10c). The contributions by St and Ns clouds to the total cloud fraction perturbation are negligible (not shown). Further analysis of CloudSat surface precipitation flags in conjunction with cloud types illustrates that precipitation associated with the BSISV is largely associated with the deep convective clouds, with the low-level Cu/Sc primarily responsible for drizzle.

It is worth mentioning that due to the sensitivity of the CPR, many warm cumulus clouds and thin cirrus clouds, consisting of relatively small particles, lack sufficiently large hydrometeors to be detected by the millimeter-wave radar, and thus are likely to be underestimated by the CloudSat (e.g., Zhang et al. 2007; Kubar et al. 2010). Also, because of possible CPR surface return contamination, shallow cumulus (e.g., fair weather) may likely be
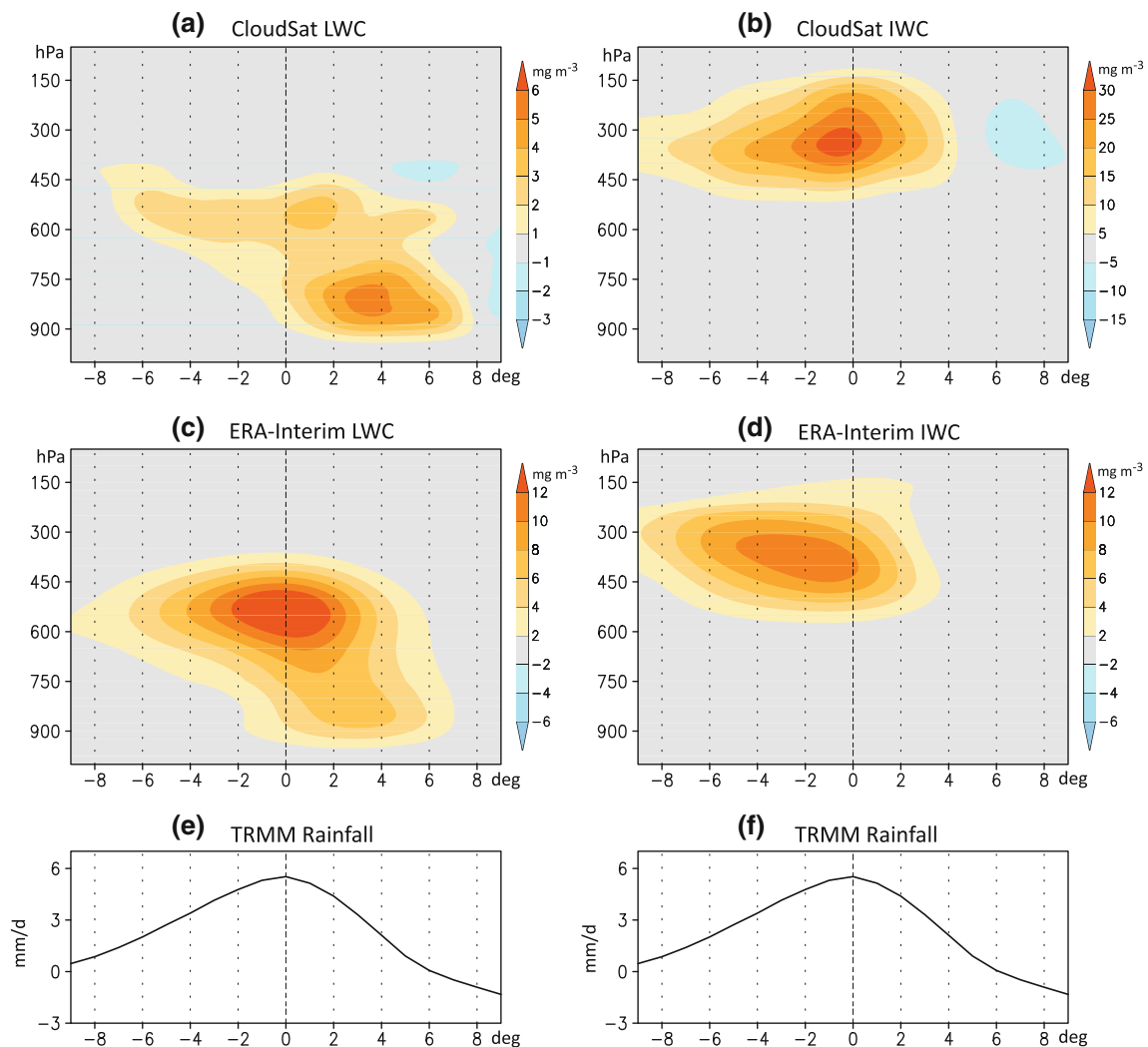
Fig. 8 Composite meridional–vertical structures of anomalous LWC (*left upper two panels*), IWC (*right upper two panels*) based on CloudSat (*upper panels*) and ERA-interim (*middle panels*). Meridional profile of the composite rainfall is also displayed in lower two panels. *X*-axis in each panel is the meridional distance (degrees of latitude) relative to the BSISV convection center. The positive (negative) values mean to the north (south). All variables are averaged over 80°–95°E

underrepresented by CloudSat (Sassen and Wang 2008). Additionally, it is expected that some mid-level cumulus congestus could be mixed in the altocumulus CloudSat cloud category in Fig. 10e, due to the overlapping definitions of cloud base between 2 and 3 km of altocumulus and cumulus clouds. Meanwhile, altostratus clouds shown in Fig. 10d may include some anvil clouds associated with deep convection, since high clouds are defined by CloudSat with bases higher than 7 km (Wang and Sassen 2007). In the tropics, Houze (1993) defines high clouds with bases above 6 km.

Regardless of these above caveats of CloudSat estimates, the transition in cloud structures associated with BSISV convection, from shallow cumuli, to deep convective clouds, and then upper anvil clouds displays great

similarity to those which have been revealed in convectively coupled equatorial waves (CCEWs), easterly waves, and the MJO (Kiladis et al. 2009). This ubiquity of vertical clouds and dynamical profiles from MCSs to planetary scale waves remains a mystery for the climate research community on the manner in which convection is coupled to the large-scale circulation (Mapes et al. 2006; Kiladis et al. 2009).

It is also noteworthy that an analogous composite analysis of ERA-interim cloud fields, but based on 33 strong BSISV events from 1998 to 2008 as identified by the approach described in Sect. 3, yields very similar anomalous cloud structures of the BSISV to those discussed above based on the 10 events during 2006–2008. It thus further lends credibility to the findings in this study.
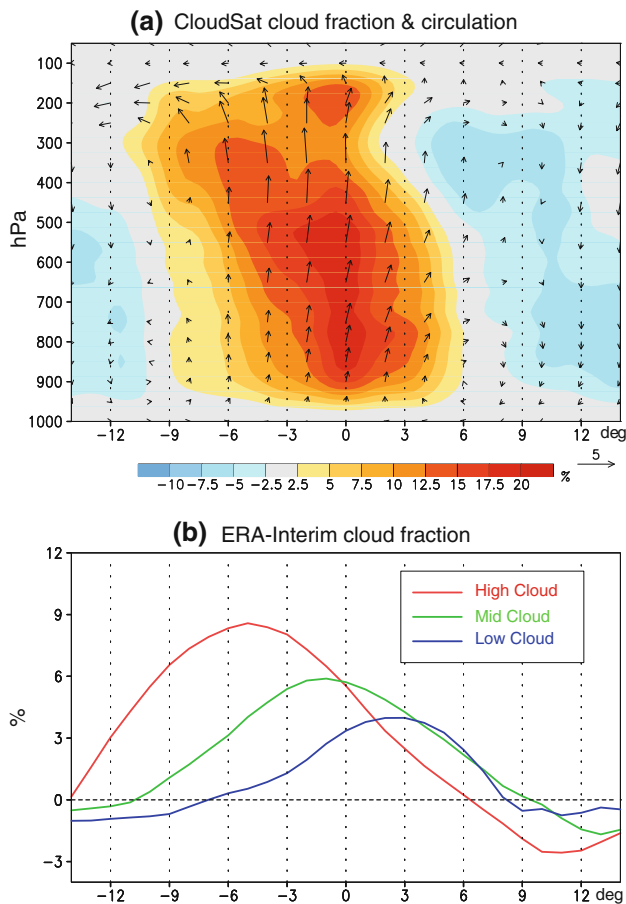
Fig. 9 a Similar as in Fig. 8a–d, but for composite anomalous cloud fractional coverage based on CloudSat (*shading*) and meridional–vertical wind vectors (see scale at lower rhs with units of ms^{-1} for v and 100 Pa s^{-1} for ω) derived from ERA-interim; **b** Similar as in Fig. 8e–f, but for anomalous cloud coverage of low (*blue*), middle (*green*), and high (*red*) level clouds from ERA-interim reanalysis

5 Summary and discussion

While the BSISV exerts significant modulation on the Asian summer monsoon, mechanisms to fully understand its behaviors are still elusive, and predictive skill for this form of variability remains limited. In order to gain insights into the physics governing the BSISV, particularly its northward propagation, we have analyzed vertical structures of cloud water content and cloud types associated with the BSISV over the Indian Ocean and subcontinent by capitalizing on the recent release of 3D cloud observations by the CloudSat mission. These cloud structures of the BSISV based on CloudSat are further compared to their counterparts derived from ERA-interim reanalysis. Of particular interest is that results based on both datasets suggest a marked asymmetric structure in cloud LWC relative to the convection center during the northward propagation of the BSISV. Increased LWC in the lower troposphere is located north of the BSISV rainfall

maximum, and therefore leads the convection. This northward displacement of increased LWC, which is in accord with local enhanced moisture as previously documented, could play a fundamental role for the northward propagation of the BSISV. Further analysis based on CloudSat estimates indicates that the enhanced LWC anomalies to the north of the BSISV convection center are largely associated with low-level cumulus/stratocumulus clouds. Differences in the anomalous LWC fields based on CloudSat and ERA-interim are also noted. The maximum LWC anomalies are detected in the lower troposphere based on CloudSat, and in the middle troposphere in the ERA-interim.

Meanwhile, analyses based on both datasets illustrate that enhanced cloud IWC is evident in the upper troposphere corresponding to enhanced BSISV convection. While a clear southward phase shift ($\sim 2°$) relative to the convection center is evident in the ERA-interim IWC field, the CloudSat IWC field shift is only weakly southward. In addition, CloudSat IWC anomalies are much stronger than the reanalysis. Further analysis based on CloudSat data indicates that the anomalous IWC pattern of the BSISV is largely associated with deep convective clouds.

While these aforementioned differences in LWC and IWC structures associated with the BSISV could be ascribed to model biases in representing convective processes and aforementioned caveats in the CloudSat retrievals, it is partially due to different IWC and LWC definitions of the model and observations. For example, as previously discussed, differences in cloud water content between ERA-interim and CloudSat estimates need to be reconciled in terms of cloud and precipitation particles. CloudSat is sensitive to both cloud and precipitation sized liquid and ice particles. As a result, retrieved estimates from CloudSat represent more than just suspended cloud liquid and ice water, which is the case for models (e.g., Waliser et al. 2009). In fact, a specific sub-sampling/filtering experiment was conducted based on CloudSat in Waliser et al. (2009), by recalculating the IWC by excluding all the retrievals flagged as either precipitating at the surface or "convective" (including the "deep convection" and "cumulus" cloud classifications). Only about 30% of profiles containing IWC in the tropics are non-convective or not associated with surface precipitation, and this filtered IWC is comparable to IWC from the GCMs. It is indicated by Fig. 10 that such "filtering" for CloudSat IWC could partially account for the difference between CloudSat and models in terms of the phase relationship between IWC and the convection center. However, larger ERA-interim LWC anomalies associated with the BSISV than those of CloudSat are still not understood, and further investigation is needed.
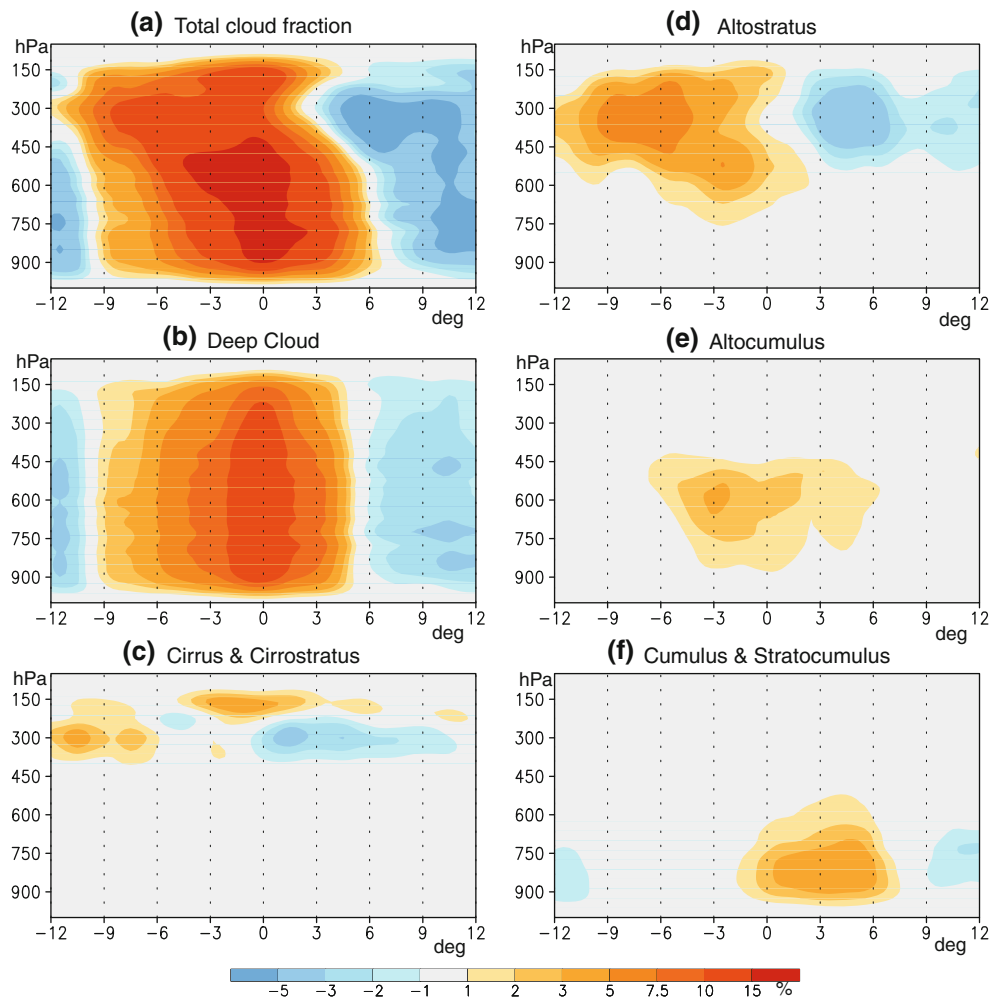
Fig. 10 Decomposition of total cloud fraction perturbation associated with the BSISV by cloud types based on CloudSat: **a** total cloud fraction (same as shading in Fig. 9a with modified color scales); **b** deep convective cloud; **c** cirrus and cirrostratus; **d** altostratus; **e** altocumulus; and **f** cumulus and stratocumulus

Another plausible explanation for the differences between CloudSat and ERA-interim datasets could be due to data sampling. The daily average cloud water fields employed in this study are based on twice daily sampling at about 1:30 pm and 1:30 am local time when CloudSat samples the Tropics. The daily fields based on the ERA-interim reanalysis contain four outputs per day, at 00, 06, 12, 18 UTC. In order to assess the impact of this sampling issue on the results, we constructed similar vertical LWC and IWC structures associated with the BSISV as in Fig. 8, but by employing only the ERA-interim outputs at 00 and 12 UTC, and 06 and 18 UTC, respectively. For the Indian Ocean BoB sector, the latter case is closer to the overpass times of CloudSat. The results suggest that the differences in the LWC and IWC structures between these ERA-interim output pairs are small (figure not shown) compared to the differences between CloudSat and

ERA-interim as shown in Fig. 9. Thus, differences in the diurnal sampling of clouds do not account for the major differences in LWC and IWC structures between CloudSat and the reanalysis.

Regardless of the differences between CloudSat and ERA-interim reanalysis, some prominent features in the cloud structures associated with the BSISV are illustrated by both datasets. In particular, the transition in cloud structures associated with the northward propagating BSISV convection, from shallow cumuli, to deep convective clouds, and then upper anvil clouds, is revealed for the first time. This vertical tilting in cloud structures greatly resembles those that have been previously found in convective systems with a wide range of scales from MCSs to planetary scale waves, which could represent a fundamental coupling process between the clouds and large-scale circulation.

References

Austin RT, Heymsfield AJ, Stephens GL (2009) Retrieval of ice cloud microphysical parameters using the CloudSat millimeter-wave radar and temperature. J Geophys Res 114. doi:10.1029/2008JD010049

Cadet DL (1986) Fluctuations of precipitable water over the Indian-Ocean during the 1979 summer monsoon. Tellus Ser A Dyn Meteorol Oceanogr 38:170–177

Chen YH, Del Genio AD (2009) Evaluation of tropical cloud regimes in observations and a general circulation model. Clim Dyn 32:355–369. doi:10.1007/S00382-008-0386-6

Drbohlav H-KL, Wang B (2005) Mechanism of the northward-propagating intraseasonal oscillation: insights from a zonally symmetric model. J Clim 18:952–972

Duchon CE (1979) Lanczos filtering in one and two dimensions. J Appl Meteorol 18:1016–1022

Fu X, Wang B, Li T, McCreary JP (2003) Coupling between northward-propagating, intraseasonal oscillations and sea surface temperature in the Indian Ocean. J Atmos Sci 60:1733–1753

Fu XH, Wang B, Tao L (2006) Satellite data reveal the 3-D moisture structure of Tropical Intraseasonal Oscillation and its coupling with underlying ocean. Geophys Res Lett 33:L03705. doi:10.1029/2005GL025074

Goswami BN (2005) South Asian monsoon. In: Lau WKM, Waliser DE (eds) Intraseasonal variability in the atmosphere–ocean climate system. Springer, Heidelberg, pp 389–424

Houze RA (1993) Cloud dynamics. Academic Press, San Diego

Houze RA (2004) Mesoscale convective systems. Rev Geophys 42. doi:10.1029/2004RG000150

Hsu H-H, Weng C-H (2001) Northwestward propagation of the intraseasonal oscillation in the western north Pacific during the boreal summer: structure and mechanism. J Clim 14:3834–3850

Hsu HH, Weng CH, Wu CH (2004) Contrasting characteristics between the northward and eastward propagation of the intraseasonal oscillation during the boreal summer. J Clim 17:727–743

Huffman GJ, Adler RF, Bolvin DT, Gu G, Nelkin EJ, Bowman KP, Hong Y, Stocker EF, Wolff DB (2007) The TRMM multisatellite precipitation analysis (TMPA): quasi-global, multiyear, combined-sensor precipitation estimates at fine scales. J Hydrometeorol 8:38–55

Jakob C, Tselioudis G (2003) Objective identification of cloud regimes in the tropical western Pacific. Geophys Res Lett 30. doi:10.1029/2003GL018367

Jiang X, Li T (2005) Reinitiation of the boreal summer intraseasonal oscillation in the tropical Indian Ocean. J Clim 18:3777–3795

Jiang X, Waliser DE (2008) Northward propagation of the subseasonal variability over the eastern Pacific warm pool. Geophys Res Lett 35. doi:10.1029/2008GL033723

Jiang X, Waliser DE (2009) Two dominant subseasonal variability modes of the eastern Pacific ITCZ. Geophys Res Lett 36:L04704. doi:10.1029/2008gl036820

Jiang X, Li T, Wang B (2004) Structures and mechanisms of the northward propagating boreal summer intraseasonal oscillation. J Clim 17:1022–1039

Johnson RH, Rickenbach TM, Rutledge SA, Ciesielski PE, Schubert WH (1999) Trimodal characteristics of tropical convection. J Clim 12:2397–2418

Kemball-Cook S, Wang B (2001) Equatorial waves and air–sea interaction in the boreal summer intraseasonal oscillation. J Clim 14:2923–2942

Kikuchi K, Takayabu YN (2004) The development of organized convection associated with the MJO during TOGA COARE IOP: trimodal characteristics. Geophys Res Lett 31:L10101. doi:10.1029/2004GL019601

Kiladis GN, Wheeler MC, Haertel PT, Straub KH, Roundy PE (2009) Convectively coupled equatorial waves. Rev Geophys 47:RG2003. doi:10.1029/2008RG000266

Kim HM, Kang IS, Wang B, Lee JY (2008) Interannual variations of the boreal summer intraseasonal variability predicted by ten atmosphere-ocean coupled models. Clim Dyn 30:485–496. doi:10.1007/S00382-007-0292-3

Kubar TL, Waliser D, Li J-L (2010) Boundary layer and cloud structure controls on tropical low cloud cover using A-Train satellite data and ECMWF analysis. J Atmos Sci (submitted)

Lau WK-M, Waliser DE (2005) Intraseasonal variability in the atmosphere–ocean climate system, Springer, Heidelberg, Germany, 474 pp

Lawrence DM, Webster PJ (2002) The boreal summer intraseasonal oscillation: relationship between northward and eastward movement of convection. J Atmos Sci 59:1593–1606

Li JL, Jiang JH, Waliser DE, Tompkins AM (2007) Assessing consistency between EOS MLS and ECMWF analyzed and forecast estimates of cloud ice. Geophys Res Lett 34:L08701. doi:10.1029/2006gl029022

Madden RA, Julian PR (1971) Detection of a 40–50 day oscillation in zonal wind in tropical Pacific. J Atmos Sci 28:702–708

Madden RA, Julian PR (1994) Observations of the 40–50-day tropical oscillation: a review. Mon Weather Rev 122:814–837

Mapes B, Tulich S, Lin J, Zuidema P (2006) The mesoscale convection life cycle: Building block or prototype for large-scale tropical waves? Dyn Atmos Oceans 42:3–29. doi:10.1016/J.Dynatmoce.2006.03.003

North GR, Bell TL, Cahalan RF, Moeng FJ (1982) Sampling errors in the estimation of empirical orthogonal functions. Mon Weather Rev 110:699–706

Rossow WB, Tselioudis G, Polak A, Jakob C (2005) Tropical climate described as a distribution of weather states indicated by distinct mesoscale cloud property mixtures. Geophys Res Lett 32:L21812. doi:10.1029/2005GL024584

Sassen K, Wang Z (2008) Classifying clouds around the globe with the CloudSat radar: 1-year of results. Geophys Res Lett 35:L04805. doi:10.1029/2007GL032591

Sikka DR, Gadgil S (1980) On the maximum cloud zone and the ITCZ over Indian, longitudes during the southwest monsoon. Mon Weather Rev 108:1840–1853

Simmons A, Uppala S, Dee D, Kobayashi S (2006) ERA-interim: New ECMWF reanalysis products from 1989 onwards, ECMWF, Shinfield Park, Reading, Berkshire RG2 9AX, UK

Stephens GL, Vane DG, Boain RJ, Mace GG, Sassen K, Wang ZE, Illingworth AJ, O'Connor EJ, Rossow WB, Durden SL, Miller SD, Austin RT, Benedetti A, Mitrescu C, Team CS (2002) The

CloudSat mission and the a-train—a new dimension of space-based observations of clouds and precipitation. Bull Am Meteorol Soc 83:1771–1790. doi:10.1175/BAMS-83-12-1771

Tromeur E, Rossow WB (2010) Interaction of tropical deep convection with the large-scale circulation in the MJO. J Clim (in press)

Waliser DE (2006) Intraseasonal variations. In: Wang B (ed) The Asian monsoon. Springer, Heidelberg, p 787

Waliser DE, Jin K, Kang IS, Stern WF, Schubert SD, Wu MLC, Lau KM, Lee MI, Krishnamurthy V, Kitoh A, Meehl GA, Galin VY, Satyan V, Mandke SK, Wu G, Liu Y, Park CK (2003) AGCM simulations of intraseasonal variability associated with the Asian summer monsoon. Clim Dyn 21:423–446. doi:10.1007/s00382-003-0337-1

Waliser D, Li J-L, Woods CP, Austin R, Bacmeister JT, Chern JD, Del Genio A, Jiang J, Kuang Z, Meng H, Minnis P, Platnick S, Rossow WB, Stephens G, Sun-Mack S, Tao W-K, Tompkins AM, Vane DG, Walker C, Wu D (2009) Cloud ice: a climate model challenge with signs and expectations of progress. J Geophys Res 114. doi:10.1029/2008JD010015

Wang B (2006) The Asian monsoon. Springer, Heidelberg

Wang B (2008) Thrusts and prospects on understanding and predicting Asian monsoon climate. Acta Meteorol Sin 22:383–403

Wang Z, Sassen K (2007) Level 2 cloud scenario classification product process description and interface control document, version 5.0, 50 pp. Available at http://www.cloudsat.cira.colostate.edu

Wang B, Xie X (1997) A model for the boreal summer intraseasonal oscillation. J Atmos Sci 54:72–86

Wang B, Webster PJ, Teng HY (2005) Antecedents and self-induction of active-break south Asian monsoon unraveled by satellites. Geophys Res Lett 32:L04704. doi:10.1029/2004GL020996

Weare BC, Nasstrom JS (1982) Examples of extended empirical orthogonal function analyses. Mon Weather Rev 110:481–485

Webster PJ (1983) Mechanisms of monsoon low-frequency variability: surface hydrological effects. J Atmos Sci 40:2110–2124

Wu DL, Austin RT, Deng M, Durden SL, Heymsfield AJ, Jiang JH, Lambert A, Li JL, Livesey NJ, McFarquhar GM, Pittman JV, Stephens GL, Tanelli S, Vane DG, Waliser DE (2009) Comparisons of global cloud ice from MLS, CloudSat, and correlative data sets. J Geophys Res 114:D00a24. doi:10.1029/2008jd009946

Yasunari T (1979) Cloudiness fluctuations associated with the northern hemisphere summer monsoon. J Meteorol Soc Jpn 57:227–242

Zhang CD (2005) Madden-Julian oscillation. Rev Geophys 43:36. RG2003, doi:10.1029/2004RG000158

Zhang YY, Klein S, Mace GG, Boyle J (2007) Cluster analysis of tropical clouds using CloudSat data. Geophys Res Lett 34:L12813. doi:10.1029/2007GL029336